Int J Appl Earth Obs Geoinformation 74 (2019) 231–238

Contents lists available at ScienceDirect

Int J Appl Earth Obs Geoinformation

journal homepage: www.elsevier.com/locate/jag

Mapping shoreline indicators on a sandy beach with supervised edge detection of soil moisture differences

H.M.A. van der Werff*

Faculty for Geo-Information Science and Earth Observation, University of Twente, Enschede 7500 AE, The Netherlands

ARTICLE INFO

Keywords:
Edge detection
Template matching
Shoreline
Indicator
Sandy beach
Schiermonnikoog

ABSTRACT

This study describes a method to map shoreline indicators on a sandy beach. The hypothesis is that, on this beach, spectral albedo is predominantly determined by moisture content and water lines can, therefore, be detected as albedo contrasts. A laboratory experiment is performed to relate moisture content to image albedo, and supervised edge detection is subsequently used to map the shoreline indicators with remote sensing imagery. The algorithm is tested with data from visible, near-infrared and shortwave-infrared wavelength regions. These results are compared to shoreline indicators obtained by a field survey and a shoreline indicator derived from a digital elevation model. Both the water line present when the imagery was acquired, as well as the maximum extent of the last flood, can be detected as a single edge. Older high water lines are confused with the last high water line and appear dispersed, as there are multiple debris lines present on the beach. The low water line, usually in saturated sand, also appears dispersed due to the presence of channels and troughs. Shorelines are constant moving boundaries, which is why shoreline indicators are used as a proxy. Unlike a mathematical indicator that is based on an elevation model, our method is more sensitive to the dynamic nature of shorelines. Supervised edge-detection is a technique for generating reproducible measurements of shoreline indicator positions over time, and aids in the monitoring of coastline migration.

1. Introduction

A shoreline, or coastline, is the physical interface between land and sea (Gens, 2010; Parker, 2002; Short, 1999). Due to the tide and long-term effects such as sea-level changes and sediment transport, the position of shorelines change continuously in time and space (Su and Gibeaut, 2017). Due to this dynamic nature, the "true" shoreline is often represented by a shoreline indicator (Boak and Turner, 2005). The definition of a shoreline thus depends on the selection of the shoreline indicator (Leatherman, 2003). Two types of shoreline indicators can be distinguished: Mathematical and physical indicators. Mathematical indicators are derived from local tide data. Physical indicators consist of morphological and non-morphological indicators. Morphological indicators relate to berm crests, scarp edges, vegetation and dunes. Non-morphological indicators relate to the water line and sand wetness. The high water line (HWL) is well recognisable on a beach and is, therefore, a frequently chosen indicator for remote sensing (Pajak and Leatherman, 2002).

Traditionally, shorelines are drawn with a visual interpretation of terrain features and aerial photographs (Leatherman, 1983). More recently, the mapping of shorelines is aided by high-spatial-resolution optical imagery, RADAR, LIDAR or combinations of topography and bathymetry (Boak and Turner, 2005). Overviews of remote sensing and image processing methods for shoreline detection are in Gens (2010) and Boak and Turner (2005). Most shoreline detection algorithms map the interface between water and land, for example Kelly and Gontza (2018) and de Sousa et al. (2018). The dynamic nature of the coast makes that the measured shoreline locations are subject to wind and tide. Obtaining a cloud-free image product often requires a merge of multiple remote sensing images, leading to an added uncertainty in the position of the coastline (Hagenaars et al., 2018).

This paper describes a novel remote sensing approach for mapping shoreline indicators on the beach. A supervised edge detection technique is applied to optical remote sensing imagery to map several water lines on a sandy beach. This method comes with the hypothesis, tested on sand samples taken from the beach, that differences in spectral albedo are primarily caused by differences in the moisture content of the sand. Along the HWL, three other water lines that are visible in the study area are mapped as well: the previous high water line (PHWL) in the backshore, the instantaneous water line (IWL), and the low water line (LWL) in the tidal plain. These results are compared with the mean high water line (MHWL) that is routinely derived from a digital

* Corresponding author.
E-mail address: harald.vanderwerff@utwente.nl.

https://doi.org/10.1016/j.jag.2018.09.007
Received 26 April 2018; Received in revised form 7 September 2018; Accepted 10 September 2018
Available online 01 October 2018

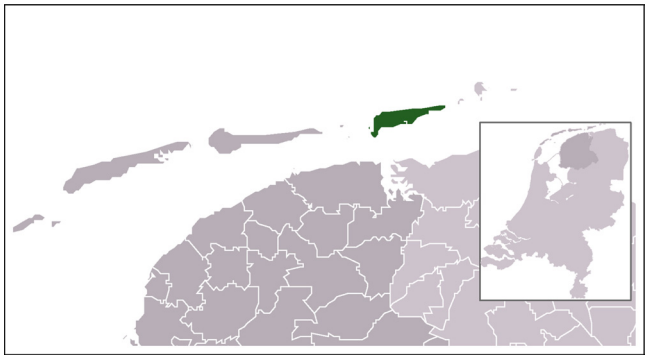

Fig. 1. Location of the island Schiermonnikoog in the north of The Netherlands. The image is copyrighted by the "Statistics Netherlands" (CBS) and is taken without modification from Wikimedia under the CC BY-SA 3.0 license.

elevation model.

2. Study area

Schiermonnikoog is a barrier island located in the north of The Netherlands between the North Sea and the intertidal Wadden Sea (Fig. 1). The 40 km^2-large island is part of a dynamic tidal area and has a mean tidal range of 2.29 m (Hollebrandse, 2005). The northern shore consists of dunes and a broad beach plain; the southern shore consists of salt marshes and tidal flats intersected by numerous creeks and channels. Erosion, transportation and sedimentation of sand by Eastward alongshore currents causes an Eastward migration of the island over time.

The area studied in this paper is on the northern shore (Fig. 2). At this location, the beach slopes 0–2%, is approximately 0.5 km wide when measured from the berm to the low tide water line, and consists of a berm, tidal plain and trough. Behind the beach is a strand-line ridge ("Rijkswaterstaat dune") which was made by planting marrow grass (*Amophila Arenaria*) to protect the sand from wind erosion. Behind the strand-line ridge are dunes. Fig. 3 gives photo impressions of these beach zones.

Fig. 4 shows shoreline indicators present on the beach of Schiermonnikoog. Two of these indicators are related to morphology and vegetation cover: The "dune line", which coincides with the dune scarp, and the "vegetation line", which is the outer limit of the vegetated beach environment. Also, there are four non-morphological indicators: the previous high water line (PHWL) in the backshore, and the high water line (HWL), instantaneous water line (IWL) and low water line (LWL) in the tidal plain. The locations of these four non-morphological indicators depend on sea state and may change within a day. Table 1 lists the physical characteristics of six beach zones that are separated by the shorelines indicators.

3. Method and data

Sand samples were acquired from the beach (Section 3.1) and analysed in a laboratory (Section 3.2) to link the moisture content to spectral albedo. First, mineral composition, organic matter and carbonate content were determined to verify that spectral albedo was not influenced by other materials that could be present in the beach sand. An artificial wetting experiment was done to determine the relationship between spectral albedo and moisture content. Then, a visible (VIS), near-infrared (NIR) and shortwave-infrared (SWIR) band were selected from an airborne hyperspectral image (Section 3.3) and subjected to a supervised edge detection algorithm (Section 3.4) to map differences in spectral albedo as a proxy for waterline indicators.

3.1. Field data

Beach sand samples were acquired on September 27th, 2006, at an incoming low tide, in between high tide at 13:45 Central European Time (CET) (108 cm above Normaal Amsterdams Peil (NAP)) and low tide at 19:55 CET (116 cm below NAP). Both days had a clear sky with no rain, similar to the conditions when the optical imagery was acquired (June 19th, 2005). The samples were acquired in 3 parallel transects that covered the beach profile from the dune crest to the LWL. In each profile, 38 samples were collected. The spacing was 30 m, except for the last 100 m to the LWL, which was sampled at a 4 m spacing as it visually showed irregular patterns in water content. Each sample location was confirmed with a "Garmin E-TREX" handheld GPS that had an estimated positional error of 5 m. The top 4 cm of the sand was taken and stored in plastic hermetic containers to preserve the original amount of moisture as best as possible. Apart from collecting samples, also the current water line was tracked twice with GPS (Section 3.5), and a description of the six beach compartments was made (Table 1).

3.2. Laboratory data

The original moisture content was determined by three times measuring the weight of the samples in a desiccator: Once in their original condition, once after drying in an oven at a temperature of 40 °C, and once after drying at a temperature of 105 °C. The obtained mass differences were recalculated to volumetric water content since photon interaction depends on volume rather than mass (Lobell and Asner, 2002).

An artificial wetting experiment was done to determine the relationship between spectral albedo and moisture content. First, water was added to the oven-dried samples until a thin layer of water was standing on the sample. The thin layer was pipetted off, and the volumetric water content was determined. The samples were subsequently dried in an oven at 40 °C, in seven stages of 1 h each. Every hour, the samples were weighed, and spectral measurements were acquired. An ASD Fieldspec FR Pro was used to collect the spectral measurements. This instrument measures in the 400–2500 nm wavelength range with a 2–3 nm spectral resolution. A high-intensity contact probe with an internal light source was pressed into each sample to ensure identical illumination conditions for all samples. Each sample was measured by averaging five measurements that were taken while moving the contact probe over the sample in between measurements. The relation between volumetric water content and spectral albedo in the VIS, NIR and SWIR wavelength ranges was found by making a linear regression.

The albedo of beach sand is not only depending on moisture content. To determine the presence of other components that could

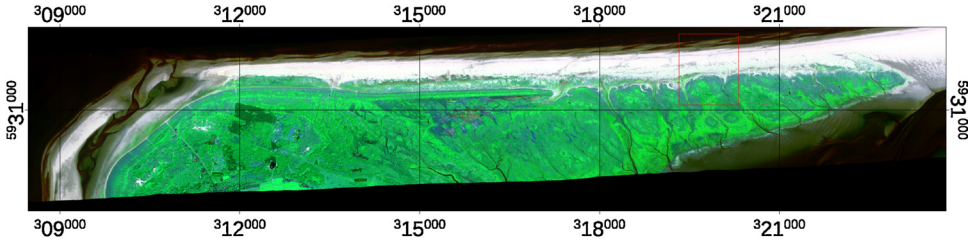

Fig. 2. The red box indicates the 0.99 × 1.31 km study area on the northern shore of Schiermonnikoog. The image is a false colour composite of red: 601 nm; green: 746 nm; blue: 1622 nm. The image has a 3.0 × 3.5 m pixel size and is projected in UTM zone 32N coordinates, shown with a 3-km grid. (For interpretation of the references to color in this figure legend, the reader is referred to the web version of this article.)

Fig. 3. Photos of the six zones in the beach profile. Zones A–C are in the vegetated area, and zones D–F are in the bare area. Photos were taken by Ms M.V. Mendez Alvez. (For interpretation of the references to color in this figure legend, the reader is referred to the web version of this article.)

influence the albedo, six composite samples that represent the different beach zones were exposed oven temperatures of 450 °C and 600 °C to determine loss of organic matter and carbonate, respectively.

3.3. Image data

Three hyperspectral images that cover the island of Schiermonnikoog were acquired on the 19th of June 2005 by the Flemish Institute for Technological Research (VITO). The time of acquisition was 10:30 CET, which fell within an incoming low tide with calm weather and sea conditions (Table 2). The images were acquired with the Advanced Hyperspectral Sensor (AHS) sensor, originally developed by the Spanish National Institute for Aerospace Technology (INTA). This whiskbroom line-scanner instrument has 80 channels with 12-bit digitisation accuracy (Table 3), a 2.5 mrad instantaneous field-of-view and a 90° field-of-view with 750 pixels per scanline (INTA, 2018).

Accumulation of ice and dirt during the flight resulted in signal degradation, leaving only the first 21 bands (0.455–1.622 μm) available for analysis. The images were radiometrically, geometrically and atmospherically corrected by VITO. An atmospheric correction based on

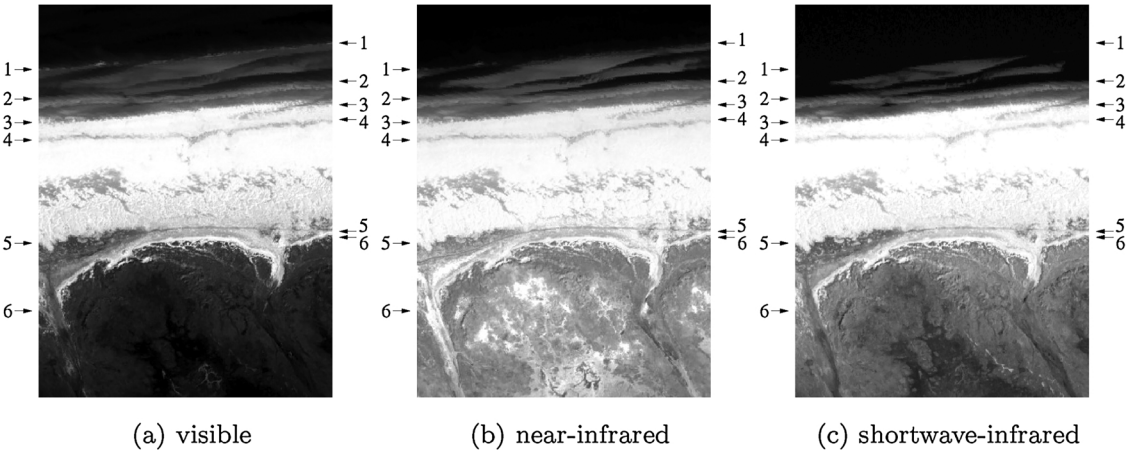

Fig. 4. The VIS (601 nm), NIR (746 nm) and SWIR (1622 nm) bands of the AHS image. The six indicated shoreline indicators in the beach profile of Schiermonnikoog are: (1) low water line; (2) instantaneous water line; (3) high water line; (4) previous high water line; (5) vegetation line; (6) dune line.

Table 1
The physical characteristics of the six zones in the beach profile. This data has been acquired during a field visit on September 27th, 2006. The recorded width of the beach zones is subject to an approximately 5 m positional error in the GPS instrument used.

Zone	Width	Description
A	> 30 m	*Dunes* – young crescent dunes with irregular surface, covered by grass except for scarps
B	158 m	*Dense vegetation* – irregular aeolian sand accumulations up to 40 cm height, covered by grass
C	93 m	*Sparse vegetation* – irregular aeolian sand accumulations up to 20 cm height, with low grass cover
D	80 m	*Wet backshore* – beach flat composed of moist compact sand with great presence of sea shells
E	109 m	*Dry backshore* – beach flat covered by dry sand, with sparse aeolian accumulations. Contains a PHWL with various shells and seaweed
F	170 m	*Foreshore* – intertidal bar intersected by channels and a trough. Contrasting dry, wet and saturated patches of sand with some ripples

Table 2
Tide and sea conditions at the time of the overflight, 19th of June 2005. High tide was 85 cm at 08:50 CET, low tide was −120 cm at 14:25 CET. The source of the tide data is a float level meter located South of Schiermonnikoog. The source of the wave data is a buoy North of Schiermonnikoog (Rijkswaterstaat, 2018).

Tide		Waves		
Time (CET)	Height (cm) [a]	Time (CET)	Height (cm) [a]	Direction (°)
10:20	57	09:00	40	50
10:30	51	10:00	37	33
10:40	45	11:00	30	20

[a] Relative to Normaal Amsterdams Peil (NAP).

Table 3
Wavelength coverage of the INTA AHS sensor (INTA, 2018). The source of this table is the University of Valencia (2018).

Wavelength coverage (μm)	Number of bands	Band width (μm)
VNIR (0.441–1.018)	20	0.030
NIR (1.491–1.650)	1	0.200
SWIR(2.019–2.448)	42	0.013
MIR (3.03–5.41)	7	0.300
LWIR (7.95–13.17)	10	0.40–0.50

MODTRAN 4 converted at-sensor radiance values to surface reflectance values. The image was initially projected in a UTM WGS-84 coordinate system with a parametric geometric correction, after which it was re-projected to the Dutch "Rijks Driehoeksmeting" coordinate system. Combined with the flight altitude resulted in a nominal pixel size of 3.0 × 3.5 m. The dataset was spatially subset to the study area, and bands 6 (601 nm), 11 (746 nm) and 21 (1622 nm) were chosen for analysis of albedo in the VIS, NIR and SWIR wavelength regions respectively. Fig. 2 shows a colour composite image of these three spectral bands.

3.4. Supervised edge detection

Originally developed for mapping boundaries in mineral assemblages (van Ruitenbeek et al., 2008; van der Werff et al., 2007), the "rotation variant template matching" technique was used to perform supervised edge detection. This approach is visualized in Fig. 5: An image template is moved over a remotely sensed image and, at each pixel location, a statistical match between the template and the image is calculated over eight (45° increments) orientations. For mapping edges, a template is a 3 × 1 pixel image. The centre pixel of this template is the axis of rotation and also points to the image coordinate where algorithm results are saved. The two remaining pixels contain the spectral signature that defines a boundary, and are called "members". At every image pixel, the fit of the template against the image is calculated for each of the eight possible orientations of the template.

The "fit of the template" (F_s) is the mean fit of all template pixels at a given position and orientation of the template:

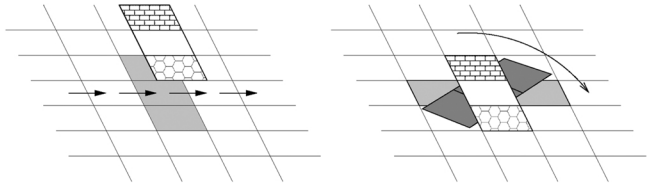

Fig. 5. The supervised edge detection algorithm matches a 3 × 1 pixel template by rotating and moving it over a remotely sensed image. The centre pixel is the axis of template rotation; the two outer pixels contain the contrasting spectral signatures that define a shoreline indicator. The fit of the template is statistically determined for every 45° orientation at every pixel of the image. This figure is taken with permission and without modification from van der Werff et al. (2007).

$$F_s = \frac{\sum_{p=0}^{N} F_{(p)}}{N} \tag{1}$$

where N is the number of template pixels.

When a crisp boundary is defined in a template, a corresponding crisp boundary in the image will give a relatively high fit to the template at orientation x, but a relatively low fit at orientation $x - 180°$, resulting in high variance in template fit measured over eight different orientations. The variance in the template fit, found while rotating the template is called "rotation variance" (V_r) and is calculated as:

$$V_r = \frac{\sum_{a=0}^{A} (F_{s(a)} - F_r)^2}{A} \tag{2}$$

where $F_s(a)$ is the spectral fit for template orientation a and F_r is the mean F_s of A rotations. V_r thus indicates the presence or absence of a crisp boundary.

When a crisp boundary is found, it needs to be known if this was caused by the presence of both template members or only one template member. The presence of only one template member in the image leads to a relatively high variance in the template fit. The variance in the spectral fit of the template ("spectral variance", V_s) is, for every orientation of the template, calculated as:

$$V_s = \frac{\sum_{p=0}^{N} (F_{(p)} - F_s)^2}{N} \tag{3}$$

The "mean spectral variance" ($\bar{V}_s$) is subsequently defined as:

$$\bar{V}_s = \frac{\sum_{a=0}^{A} V_{s(a)}}{A} \tag{4}$$

and indicates if only one member is present at a given pixel location, or that both or neither are present.

When three measures of the algorithm F_s, V_r and $\bar{V}_s$ are combined, we obtain an indicator that tells us whether none, only one, or both members are present at a specific image location. These measures are easiest interpreted when displayed together in an RGB colour composite: Red tones indicate a crisp boundary, black tones indicate that both template spectra were present, blue tones indicate that only one of the

template spectra was present, and green tones indicate that none of the template spectra was present (van der Werff et al., 2007).

3.5. Application and validation

Using the regressions of the artificial wetting experiment (Section 3.2), the AHS image values were converted from reflectance (%) to volumetric water content (%). The templates were made according to volumetric water differences found in the field data (Section 3.2). As albedo rather than colour defines the spectral contrast of each of these shoreline indicators, "intensity difference" (Bakker and Schmidt, 2002) was used as a similarity criterion in the supervised edge detection.

The detection results were compared to the MHWL shoreline indicator, which is determined by the 0 m elevation contour of the Actueel Hoogte-bestand Nederland (AHN) elevation model (AHN, 2018). During the fieldwork, the water lines were surveyed twice with a "Garmin E-TREX" handheld GPS: At low tide (07:40 CET, water level 121 cm below NAP) and high tide (13:45 CET, water level 114 cm above NAP).

4. Results

Four shoreline indicators can be defined in terms of albedo differences, being a proxy for moisture content differences. Table 4 shows the materials in each beach zone (Table 1) that could influence albedo: It appears that all samples are composed of a well sorted fine sand, and organic matter and carbonate content are less than 1%. A 5–15% water content can be observed in the foreshore (zone F), the vegetated area (zones B and C) and the wet backshore (zone D). The dry backshore (zone E) has an average water content of less than 1%.

The laboratory spectra acquired on the six composite samples are shown in Fig. 6. Apart from water absorption features at the 1.4–1.5 µm and 1.9–2.1 µm wavelength intervals, the spectra do not have significant absorption features. While these water absorption features appear to be shallow in the dune area (zone A) and the dry backshore (zone E), they are distinctly present in the spectral signatures of all other zones. From the soils in the vegetated beach area, the dunes (zone A) have the highest reflectance. Reflectance is lower in the sparsely vegetated (zone C) and densely vegetated (zone B) areas. The two zones closest to the water (E and F) have no vegetation growth. It can be seen from Fig. 6 that the reflectance in zone E (dry foreshore) is as high as the reflectance in the dunes (zone A). The wet foreshore in zone F, on the other hand, has high amounts of moisture in the sand and has, therefore, the lowest reflection of all.

The results of the artificial wetting experiments that relate moisture content to albedo by linear regression are in Fig. 7a and b. The reflectance values at 601 nm, 746 nm and 1622 nm show, when measured over eight different stages of drying, a linear relation with volumetric water content:

$$V_w = -1.68*(R_{0601} - 0.37) \qquad (r^2 = 0.99,\ n = 8) \tag{5}$$

$$V_w = -1.56*(R_{0746} - 0.40) \qquad (r^2 = 0.99,\ n = 8) \tag{6}$$

Table 4
Beach sand composition in the six zones of the beach profile, measured in 38 samples acquired with a 30 m spacing in zones A–D and a 4 m spacing in zones E and F. The recorded width of the beach zones is subject to an approximately 5 m positional error in the GPS instrument used.

Zone	A	B	C	D	E	F
Zone width (m)	30	158	93	80	109	180
Sample spacing	30	30	30	30	4	4
Number of samples	2	5	3	3	21	4
Water (%)	0.11	9.72	5.65	8.12	0.54	13.7
Carbonate (%)	0.55	0.50	0.50	0.60	0.42	0.37
Organic (%)	0.06	0.12	0.07	0.12	0.08	0.09

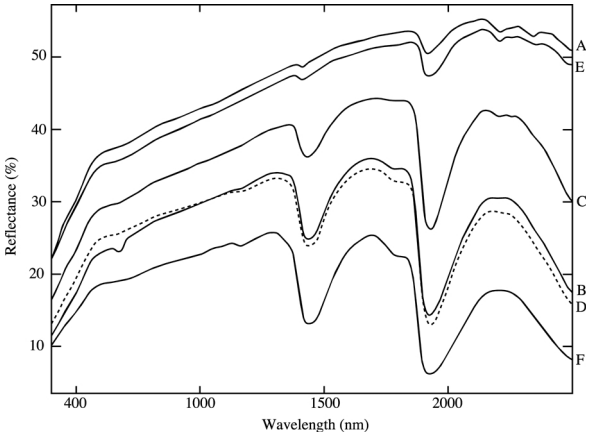

Fig. 6. Laboratory spectra of 6 composite sand samples representing the beach zones: (A) dunes, (B) dense vegetation, (C) sparse vegetation, (D) wet backshore, (E) dry backshore, and (F) foreshore.

$$V_w = -1.00*(R_{1622} - 0.56) \qquad (r^2 = 0.98,\ n = 8) \tag{7}$$

with V_w being the volumetric water content and R_{601}, R_{746} and R_{1622} the reflectance values at 601 nm, 746 nm and 1622 nm respectively.

Table 5 shows the edge criteria of the four shoreline indicators as used in the supervised edge detection. Fig. 8 shows the edge detection results, applied to the 601 nm, 746 nm and 1622 nm bands of the AHS image. Red tones indicate a crips boundary, black tones indicate that both template spectra were present, blue tones indicates that only one of the template spectra was present, and green tones indicate that none of the template spectra is present. Crisp boundaries are found in the results of all three wavelength regions, although the shoreline indicators obtained in the SWIR are visually more crisp than those obtained in the VIS and NIR.

Fig. 9 shows a cross-section of "rotation variance" values of the 601 nm band, covering the bare soil part of the beach profile. From this figure can be observed that the PHWL is detected, but also that it gets confused with the HWL. The profile of the HWL shows a distinct peak, with a minor echo of the LWL indicator. The profiles of the IWL and the LWL show more noise than the HWL profile but show distinct peaks for the shoreline indicator as well.

Fig. 10 shows a visual comparison of the location of several shoreline indicators. The HWL obtained with edge detection coincides with the location of the MHWL obtained with the AHN elevation model but is consistently located 1–2 pixels (approximately 3–7 m) landwards of the MHWL. The HWL obtained with the field GPS survey deviates on average 3–4 pixels (approx. 10–14 m) from the HWL indicator derived with edge detection, predominantly towards land. The LWL's obtained by edge detection and by GPS coincide on the edge of the foreshore with the open sea, but edge detection follows the micro-relief of the foreshore while the GPS LWL has followed a continuous straight line.

5. Discussion

Supervised edge detection is used on optical remote sensing data to map four shoreline indicators in the sandy part of the beach: The previous high water line (PHWL); the high water line (HWL), the instantaneous water line (IWL) and the low water line (LWL). These indicators are defined by contrasts in the moisture content of the beach sand, based on the hypothesis that albedo is a proxy for volumetric water content (Eqs. (5)–(7)).

The HWL is depicted in the VIS, NIR and SWIR wavelength regions. The IWL appears more clearly in the SWIR than in the VIS or NIR. The IWL location has however false anomalies in the SWIR, and the results of the VIS wavelength region seems to be better. The LWL does not appear as a single line, as it reflects the micro-relief of the foreshore:

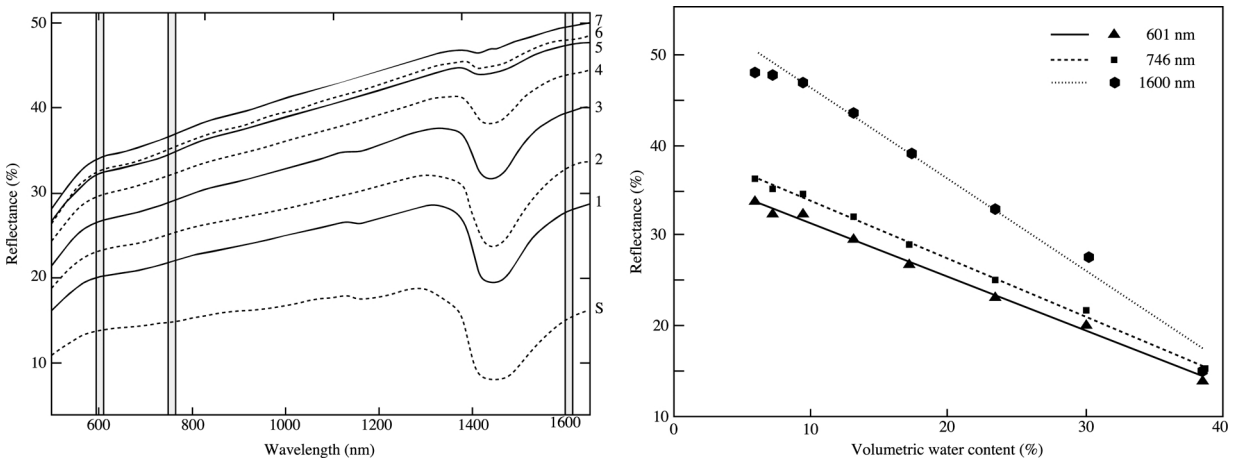

Fig. 7. (a) Laboratory spectra of soil samples that, after artificial wetting, were oven dried at 40 °C, in seven increments of 1 h each. The spectrum of the saturated sample is indicated with *S*. (b) Regressions between spectral reflectance and volumetric moisture content.

Table 5
Templates used to detect the four non-morphological shoreline indicators.

Indicator	Template endmembers			
Previous High Water Line (PHWL)	Dry	< 10%	Moist	10–20%
High Water Line (HWL)	Moist	10–20%	Wet	20–30%
Instantaneous Water Line (IWL)	Wet	20–30%	Saturated	30–40%
Low Water Line (LWL)	Saturated	30–40%	Sea	> 40%

there was an incoming low tide at the time of image acquisition, which has exposed intertidal bars and troughs. The PHWL is detected in all three wavelength regions but gets confused with the HWL. The PHWL is possibly littered with washed up materials. This shoreline indicator, therefore, cannot be defined by moisture and brightness differences only without giving false anomalies. Using a longer (e.g. 5 × 1 pixels) or wider (e.g. 3 × 3 pixels) template would lead to a reduction of false anomalies. A consequence of using bigger templates for edge detection is that the detected edge also becomes bigger. When using a 3 × 1 pixel template, the width of a detected edge is two pixels (one image pixel on each side of the actual edge). A 5 × 1 pixels template would result in an edge of 4 pixels wide, and so on. Noise reduction is a tradeoff with the width of the edge detected.

Light is transmitted through water in the VIS wavelength range but gets absorbed in the NIR and SWIR wavelength range. In general, shoreline indicators appear more crisp in the SWIR than in the VIS or NIR wavelength region (Fig. 8). Especially the IWL, detected by a “wet sand–saturated sand” template, does not appear crisp in the VIS. The black and blue tones surrounding the shoreline indicator in Fig. 8 indicate that both members of the template were present but mixed.

A comparison with reference datasets (Fig. 10) shows that the HWL is demarcated as a straight line. Spatially, the HWL that is obtained with edge detection is at most 7 m off from the MHWL that is obtained with the AHN elevation model, and at most 14 m off from the GPS survey done at high tide. Uncertainty in GPS location, as well as the error in the geometric correction of the optical image, leaves an unknown error which could cause the difference. However, the difference can also find its origin in the time of acquisition of each dataset. The indicator derived by LIDAR is the MHWL – mean high water line, which by definition is not the same as any of the shorelines we detect. The MHWL could be the same as the IWL if data acquisition would happen at the same time. For a GPS track counts the same as the MHWL, it is comparable only when acquired at the time of image acquisition. As the AHN has no information from below sea level, the detected LWL line can only be compared to the GPS survey done at low tide. Although these two lines are roughly located in the same distance from the beach, there is still a difference in time of data acquisition, interference of the actual water line (depicted by the IWL) and a continuous change in the location of bars. All in all, shoreline indicators are difficult to compare when not measured at the same time. Our method should be considered as a method that maps an alternative shoreline, that cannot be mapped with e.g. LIDAR. The possibility to map shorelines other than the water-land interface gives therefore more flexibility when monitoring coastline migration over time.

Spectral albedo measurements taken by the hand-held spectroradiometer are not only influenced by water content, but also by mineralogy, carbonate content and organic matter content. The laboratory analysis shows that organic matter and carbonate content is less than 1%. Although 1% organic matter ought to be visible in these spectral measurements (USGS Spectroscopy Lab, 2018), the 0.98 and higher r^2 values of the regression functions indicate that its influence is, at least in this study, negligible. The relationship between spectral albedo and volumetric water is logical: The spectrum of dry sand has a higher reflectance in the SWIR than in the VNIR (Fig. 6), and the albedo of dry samples is, therefore, highest at 1.6 µm and lowest at 0.6 µm. Water absorbs more light at longer wavelengths than at shorter wavelengths. The 1.6 µm band consequently has a lower albedo for saturated samples than the 0.6 µm. The resulting inverse relationship expressed in Eqs. (5)–(7)) therefore have a similar trend but a different slope.

The obtained relations between spectral albedo and volumetric water are however only valid for this particular beach sand: Other beaches may have different mineralogy or organic matter contents and therefore posses a different relation between moisture contents and spectral albedo. In case of non-contact measurements, such as done with airborne or spaceborne remote sensing, the spectral albedo is not only influenced by ground cover, but also by solar elevation, and scattering and absorption in the atmosphere. In the case of the AHS image used in our study, these corrections were all done by the data supplier (VITO).

A hyperspectral instrument is not needed for this kind of study; a broadband sensor would do just as well. A relatively high spatial resolution, however, is needed to depict spectral contrasts between beach compartments. Satellite sensors suitable for this kind of application are therefore high-spatial resolution instruments such as the Ikonos, Quickbird and Worldview series. For the application described in this paper, a sensor needs to be calibrated to reproduce surface brightness values, and a correction for atmosphere and light source is required as well. Permanent reflectors could be used to calibrate a dataset as well, which would allow the use of terrestrial imaging systems.

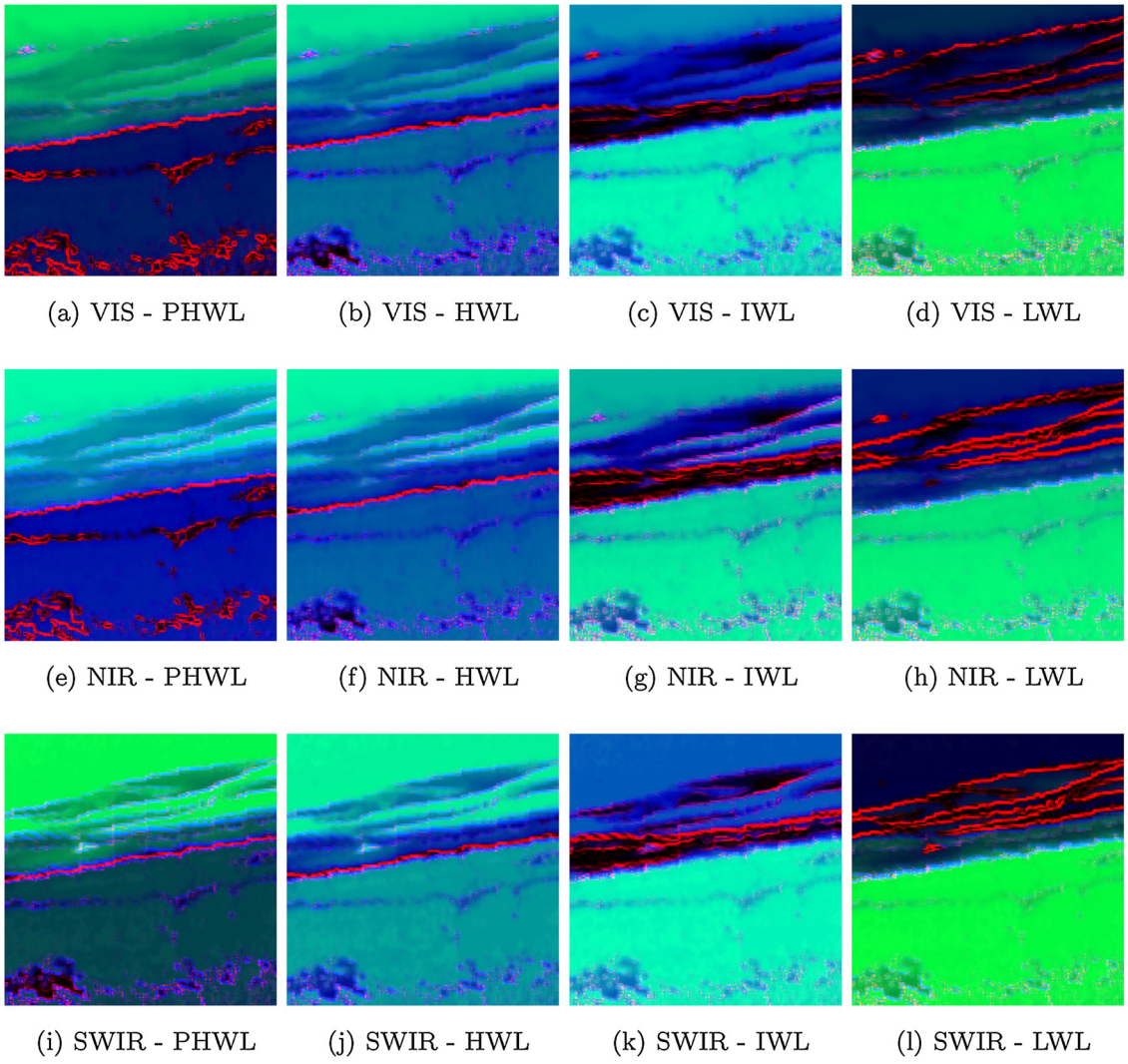

Fig. 8. RGB colour composites of the edge detection measures: "rotation variance" (V_r) in red, "mean template fit" (F_s) in green and "mean spectral variance" ($\bar{V}_s$) in blue. The interpretation of resulting colours in the composite is: crisp boundaries; both template signatures are present; only one of the template signatures is present; and none of the signatures is present. (For interpretation of the references to colour in this figure legend, the reader is referred to the web version of this article.)

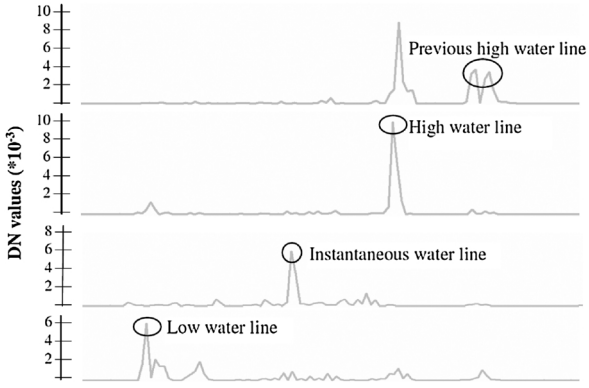

Fig. 9. Rotation variance values of the "RTM" supervised edge detection algorithm, as measured along the beach profile.

6. Conclusions

In this paper, a novel method to map shoreline indicators on a sandy beach is introduced. The technique chosen to do supervised edge detection, template matching, has been developed for mapping mineral contrasts, but it can also detect the HWL, IWL and LWL in the beach sand of Schiermonnikoog. These shoreline indicators are compared to two other indicators, obtained by a field survey and a shoreline indicator derived from a digital elevation model. The positional error falls within the error that can be expected from the spatial accuracy of the instruments used and possible changes that may have occurred over time.

On this particular beach, spectral albedo is predominantly determined by moisture content, which allows mapping of these water lines. Testing data from visible, near-infrared and shortwave-infrared wavelength regions shows that the use of longer wavelengths leads to the detection of crisp edges near the instantaneous waterline. Still, the technique can be applied to data acquired in visible light as well.

Shorelines are constant moving boundaries, which is why shoreline indicators are used as a proxy. Most algorithms for detecting shoreline indicators map the interface between water and land. A mathematical indicator based on an elevation model, however, cannot accommodate the dynamic nature of shorelines. A shoreline indicator based on the land-water interface is always subject to the tide, and thus to the time of image acquisition. When using edge detection for mapping shorelines on a beach, the HWL, IWL and LWL could be used to monitor the constantly changing locations. Remote sensing data can readily be

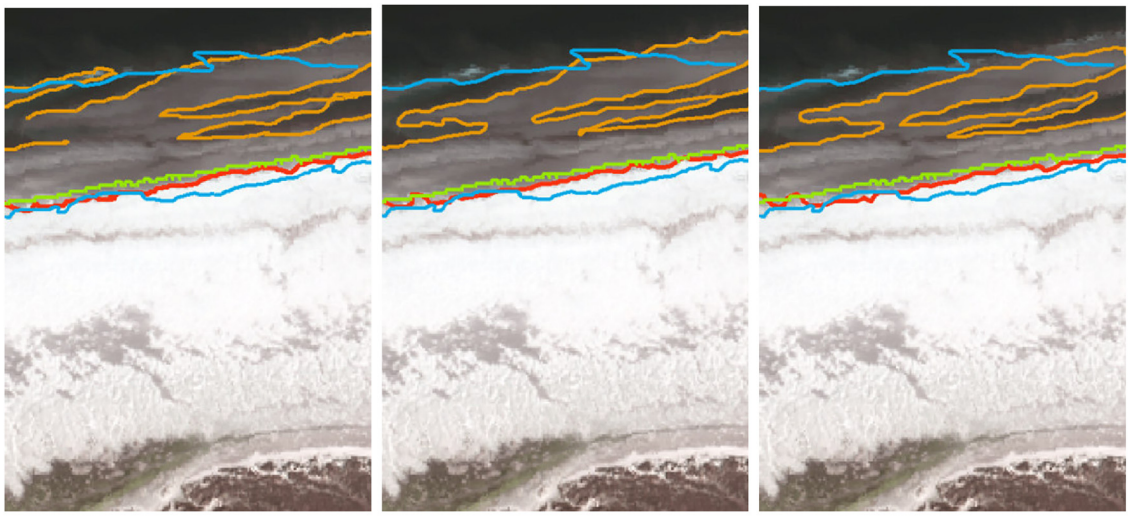

(a) visible (b) near-infrared (c) shortwave-infrared

Fig. 10. Indicators of (red) high water line and (orange) low water line derived with supervised edge detection, compared to a (blue) GPS derived indicators of high water line and low water line and a (green) LIDAR-derived indicator of the mean high water line. (For interpretation of the references to color in this figure legend, the reader is referred to the web version of this article.)

acquired more frequently, and terrestrial cameras would even allow continuous monitoring of shoreline indicators. Supervised edge-detection is a technique for generating reproducible measurements of shoreline indicator positions over time.

Acknowledgements

This paper is based on MSc research done by Ms Maria V. Méndez Alves; she is much acknowledged for doing the data analysis, conducting the fieldwork and for contribution to discussions. Michiel Damen (University of Twente) reviewed MSc thesis on this research, and Boudewijn de Smeth (University of Twente) guided the laboratory analysis.

References

AHN, 2018. Actueel Hoogtebestand Nederland. (in Dutch). http://www.ahn.nl. (Accessed on 2018-04-10).

Bakker, W., Schmidt, K., 2002. Hyperspectral edge filtering for measuring homogeneity of surface cover types. ISPRS J. Photogram. Remote Sens. 56, 246–256.

Boak, E., Turner, I., 2005. Shoreline definition and detection: a review. J. Coast. Res. 21 (4), 688–703.

de Sousa, W., Souto, M.V.S., Matos, S., Duarte, C., Salgueiro, A., da Silva Neto, C., 2018. Creation of a coastal evolution prognostic model using shoreline historical data and techniques of digital image processing in a GIS environment for generating future scenarios. Int. J. Remote Sens. 39 (13), 4416–4430.

Gens, R., 2010. Remote sensing of coastlines: detection, extraction and monitoring. Int. J. Remote Sens. 31 (7), 1819–1836.

Hagenaars, G., de Vries, S., Luijendijk, A., de Boer, W., Reniers, A., 2018. On the accuracy of automated shoreline detection derived from satellite imagery: a case study of the sand motor mega-scale nourishment. Coast. Eng. 133, 113–125.

Hollebrandse, F., June 2005. Temporal development of the tidal range in the southern North Sea (Master's thesis). Faculty of Civil Engineering and Geosciences, Delft University of Technology, Delft, The Netherlands.

INTA, 2018. Airborne Hyperspectal Scanner. (in Spanish). http://www.inta.es/opencms/export/sites/default/ICTS-PAI/es/instalaciones/segmento-aereo/instrumentacion-embarcada/instrumentacion-embarcada-para-teledeteccion-aerea/, Instituto Nacional de Técnica Areoespacial (www.inta.es). (Accessed on 2018-07-11).

Kelly, J., Gontza, A., 2018. Using GPS-surveyed intertidal zones to determine the validity of shorelines automatically mapped by Landsat water indices. Int. J. Appl. Earth Obs. Geoinf. 65, 92–104.

Leatherman, S., 1983. Shoreline mapping: a comparison of techniques. Shore Beach 28–33.

Leatherman, S., 2003. Shoreline change mapping and management along the US East Coast. J. Coast. Res. 5–13.

Lobell, D., Asner, G., 2002. Moisture effects on soil reflectance. Soil Sci. Soc. Am. J. 66 (3), 722–727.

Pajak, M., Leatherman, S., 2002. The high water line as shoreline indicator. J. Coast. Res. 18 (2), 329–337.

Parker, B., 2002. The difficulties in measuring a consistently defined shoreline – the problem of vertical referencing. J. Coast. Res. 44–56.

Rijkswaterstaat, 2018. Getij. Website by the Ministry of Infrastructure and the Environment. (in Dutch). https://www.rijkswaterstaat.nl/water/waterdata-en-waterberichtgeving/waterdata/getij/index.aspx. (Accessed on 2018-04-10).

Short, A., 1999. Handbook of Beach and Shoreface Morphodynamics. Wiley & Sons, New York, pp. 379.

Su, L., Gibeaut, J., 2017. Using UAS hyperspatial RGB imagery for identifying beach zones along the South Texas coast. Remote Sens. 9 (159).

University of Valencia, 2018. Airborne Hyperspectal Scanner. (in English). https://www.uv.es/leo/sen2flex/ahs.htm, Universitat de València (www.uv.es). (Accessed on 2018-09-06).

USGS Spectroscopy Lab, 2018. Spectroscopy of Rocks and Minerals, and Principles of Spectroscopy. , figure 19. (Accessed on 2018-04-10). https://speclab.cr.usgs.gov/PAPERS.refl-mrs/refl4.html#section4.1.

van der Werff, H., van Ruitenbeek, F., van der Meijde, M., van der Meer, F., de Jong, S., Kalubandara, S., 2007. Rotation invariant template matching for supervised hyperspectral boundary detection. IEEE Geosci. Remote Sens. Lett. 4 (1), 70–74.

van Ruitenbeek, F., van der Werff, H., Hein, K., van der Meer, F., 2008. Detection of predefined boundaries between hydrothermal alteration zones using rotation-variant template matching. Comput. Geosci. 34 (12), 1815–1826.